

Strain-Induced Modulation of Electron Mobility in Single-Layer Transition Metal Dichalcogenides MX_2 ($M = \text{Mo}, \text{W}; X = \text{S}, \text{Se}$)

Manouchehr Hosseini, Mohammad Elahi, Mahdi Pourfath, *Senior Member, IEEE*, and David Esseni, *Fellow, IEEE*

Abstract—In this paper, the effect of biaxial strain on the mobility of single-layer transition metal dichalcogenides (MoS_2 , MoSe_2 , WS_2 , and WSe_2) is investigated by accounting for the scattering from intrinsic phonon modes, remote phonons, and charged impurities. *Ab initio* simulations are employed to study a strain-induced effect on the electronic bandstructure, and the linearized Boltzmann transport equation is used to evaluate the low-field mobility. The results indicate that tensile strain increases the mobility. In particular, a significant increase in the mobility of single-layer MoSe_2 and WSe_2 with a relatively small tensile strain is observed. Under a compressive strain, however, the mobility exhibits a nonmonotonic behavior. With a relatively small compressive strain, the mobility decreases and then it partially recovers with a further increase in the compressive strain.

Index Terms—Boltzmann transport equation (BTE), mobility, strain, transition metal dichalcogenides (TMDs).

I. INTRODUCTION

GRAPHENE is the most prominent of 2-D material that is attractive for use in the next-generation nanoelectronic devices because of its high mobility [1], [2]; however, the absence of an energy gap seriously jeopardizes the usage of this material for some important electronic applications, including digital circuits [3], [4]. Other 2-D materials with nonzero bandgap, such as single and few layers of transition metal dichalcogenides (TMDs) offer promising electrical and optical properties for future electronic applications [5]. Because of the weak interlayer van der Waals bonds in the layered structure, the single to few layers of these materials can be easily obtained by mechanical or chemical exfoliation techniques [6]–[8]. The n-type FETs based on the TMDs have demonstrated a high $I_{\text{ON}}/I_{\text{OFF}}$ ratio, a relatively steep subthreshold swing, and an extremely small

OFF-current [9]–[13]. A possible application of these materials to heterojunction interlayer tunneling FETs has also been proposed and theoretically investigated [14].

The effect of strain on the bandstructure and bandgap of some of these materials has been investigated in previous studies [15], [16], and it has been shown that the application of compressive and tensile biaxial strain results in an indirect bandgap [17]–[19]. We have recently studied the effect of strain on the mobility of single-layer MoS_2 and shown that the tensile biaxial strain can significantly enhance the mobility [20]; however, the investigation of a strain effect on the mobility of other TMDs is still missing. The electronic bandstructures of the TMDs are similar, but the valleys have different effective masses and energy minima. In this paper, we present a comprehensive analysis on the effect of strain on the mobility of several TMDs, employing the first *ab initio* simulations for bandstructure calculations and then the linearized Boltzmann transport equation (BTE) for evaluating the mobility [21]. The methodology for *ab initio* calculations, scattering rates, and the discretization method of the linearized BTE is briefly presented in Section II. The effects of biaxial strain on the bandstructure and mobility of MoS_2 , MoSe_2 , WS_2 , and WSe_2 are discussed in Section III, and the concluding remarks are presented in Section IV.

II. MODELING APPROACH

This section explains the approach for the evaluation of the electronic bandstructure and mobility.

A. Bandstructure

For bandstructure calculations, we employed the density-functional theory (DFT) along with the local density approximation as implemented in the SIESTA code [22]. A 30 Å vacuum region has been used to isolate the single layer from other layers to ensure no interactions between them, thus making our calculations effectively representative of an isolated 2-D layer. A cutoff energy equal to 400 Ry was used and the sampling of the reciprocal space Brillouin zone (BZ) is performed by a Monkhorst-pack grid of $18 \times 18 \times 1$ k -points. Calculations begin with the determination of the optimized geometry, that is the configuration in which the residual Hellmann–Feynman forces acting on atoms are smaller than 0.01 eV/Å. The calculated lattice constants of an unstrained single-layer MoS_2 , MoSe_2 , WS_2 , and WSe_2

Manuscript received June 5, 2015; revised July 22, 2015; accepted July 25, 2015. Date of publication August 10, 2015; date of current version September 18, 2015. This work was supported by the Iran National Science Foundation. The review of this paper was arranged by Editor H. Jaouen.

M. Hosseini and M. Elahi are with the School of Electrical and Computer Engineering, University of Tehran, Tehran 14395-515, Iran.

M. Pourfath is with the School of Electrical and Computer Engineering, University of Tehran, Tehran 14395-515, Iran, and also with the Institute for Microelectronics, Technische Universität Wien, Vienna A-1040, Austria (e-mail: pourfath@ut.ac.ir).

D. Esseni is with the Dipartimento di Ingegneria Elettrica Gestionale e Meccanica, University of Udine, Udine 33100, Italy (e-mail: david.esseni@uniud.it).

Color versions of one or more of the figures in this paper are available online at <http://ieeexplore.ieee.org>.

Digital Object Identifier 10.1109/TED.2015.2461617

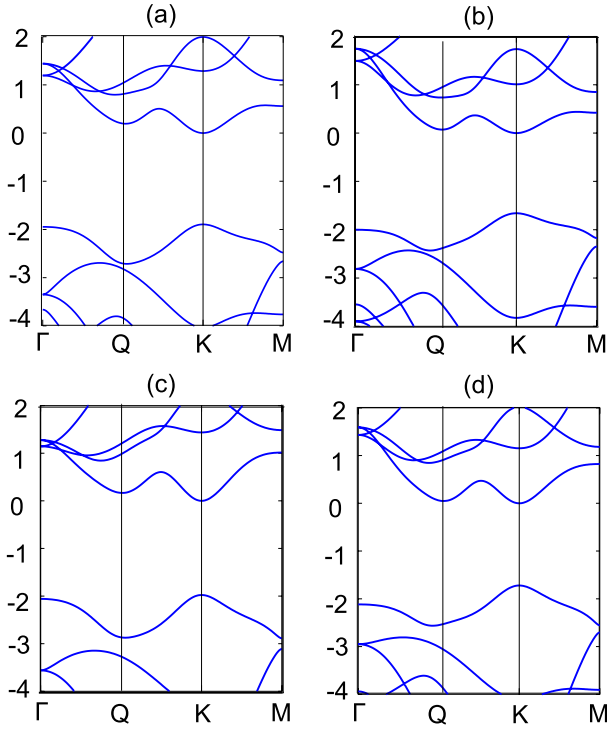


Fig. 1. Electronic bandstructure along high symmetry lines of unstrained single layer. (a) MoS₂. (b) MoSe₂. (c) WS₂. (d) WSe₂.

are 3.12, 3.24, 3.14, and 3.26 Å, respectively, which are in agreement with previously reported values in [23].

Fig. 1(a)–(d) shows that all the considered materials have a direct bandgap in the absence of strain and the energy bandgaps for MoS₂, MoSe₂, WS₂, and WSe₂ are evaluated to be 1.89, 1.66, 1.98, and 1.72 eV, respectively, which are close to the values reported in [23]. The lowest and the second lowest band minima in the conduction band are denoted as *K*- and *Q*-valleys [see Fig. 2(a)], respectively, and the energy distances between these valleys are evaluated to be 195 meV, 72 meV, 166 meV, and 48 meV, for the unstrained single-layer MoS₂, MoSe₂, WS₂, and WSe₂, respectively. A fairly wide range of values for the energy distance between the *K*- and *Q*-valleys has been reported in previous theoretical studies [23]–[25], and unfortunately no experimental verification has been yet reported except for MoS₂ [26].

B. Scattering Mechanisms and Mobility Calculation

In our calculations, carrier scattering due to the intrinsic phonons (including acoustic and optical phonons), remote phonons, and charged impurities are taken into account. Piezoelectric coupling to the acoustic phonons has been instead neglected in this paper because it is only important at low temperatures [27]. We assume that an electron envelope wave function in 2-D semiconductors can be written as $\Psi_{\vec{k}}(\vec{r}, z) = \chi(z) \exp(i\vec{k} \cdot \vec{r}) / \sqrt{S}$ with $\chi(z) = ((2/a))^{1/2} \sin(\pi z/a)$, where \vec{r} is the in-plane position, z is the direction normal to the 2-D layer, a is the thickness of the TMD single layer [28], S is the area normalization factor, and \vec{k} is the in-plane wave vector;

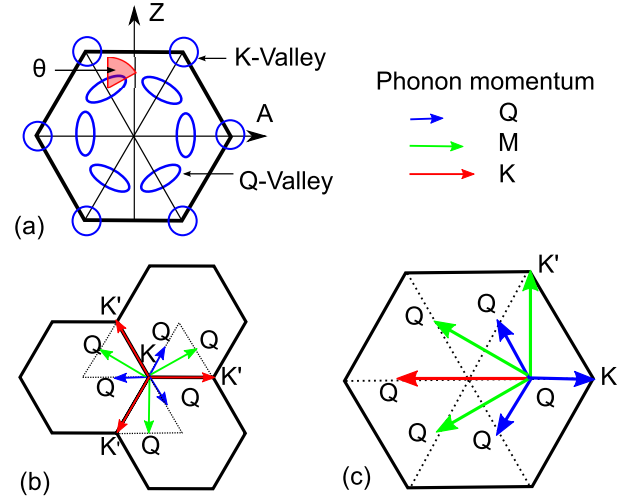


Fig. 2. (a) *K*- and *Q*-valleys in the first BZ of TMDs. The angle θ describes the *Q*-valley's orientation in \vec{k} -space. It should be noted that the zigzag direction in \vec{k} -space corresponds to the armchair direction in real space. Illustration of several phonon-assisted intervalley transitions in single-layer MX₂ for (b) transitions from *K*-valley to other valleys and (c) transitions from *Q*-valley to other valleys. The figure sets the notation used in Table I to identify phonon-assisted transitions.

throughout this paper we used $a = 0.65$ nm [9]. By assuming Fermi's golden rule, the scattering rate from an initial state \vec{k} in a valley v to a final state \vec{k}' in a valley w can be written as

$$S^{v,w}(\vec{k}, \vec{k}') = \frac{2\pi}{\hbar} |M^{v,w}(\vec{k}, \vec{k}')|^2 \delta[E^w(\vec{k}') - E^v(\vec{k}) \mp \hbar\omega(q)] \quad (1)$$

where $|M^{v,w}(\vec{k}, \vec{k}')|$ is the matrix element for the mentioned transition and $\hbar\omega(q)$ is the phonon energy that may depend on $q = |\vec{k} - \vec{k}'|$. The intravalley transitions ($v = w$) assisted by the acoustic phonons can be approximated as elastic and the rate is given by

$$S_{ac}(\vec{k}, \vec{k}') = \frac{2\pi k_B T D_{ac,1}^2}{\rho S \hbar v_s^2} \delta[E(\vec{k}') - E(\vec{k})] \quad (2)$$

where k_B is the Boltzmann constant, T is the absolute temperature, $D_{ac,1}$ is the first-order acoustic deformation potential. ρ is the mass density that is 3.1, 4.6, 4.9, 6.2 [10⁻⁷ gr/cm²] and v_s is the sound velocity that is 6.6, 4.1, 4.3, 3.3 [10³ m/s] for single-layer MoS₂, MoSe₂, WS₂, and WSe₂, respectively [30], [31]. On the other hand, the rate of inelastic phonon scattering, including intra and intervalley optical phonons, and intervalley acoustic phonons, can be expressed as

$$S_{ac/op}^{v,w}(\vec{k}, \vec{k}') = \frac{\pi (D_{ac/op,0}^{v,w})^2}{\omega_{ac/op} \rho S} \times \left[n_{op} + \frac{1}{2} \mp \frac{1}{2} \right] \delta[E^w(\vec{k}') - E^v(\vec{k}) \mp \hbar\omega_{ac/op}(q)] \quad (3)$$

where $D_{ac/op,0}^{v,w}$ is the zero-order acoustic/optical deformation potential for a transition between the valleys v and w , $\hbar\omega_{ac/op}(q)$ is the phonon energy, and n_{op} is the phonon occupation (upper and lower signs denote phonon absorption and phonon emission, respectively). There are six *Q*-valleys in the first BZ and phonon-assisted intervalley transitions

TABLE I

DEFORMATION POTENTIALS AND PHONON ENERGIES FOR PHONON-ASSISTED TRANSITIONS IN SINGLE-LAYER MoS₂, MoSe₂, WS₂, AND WSe₂. THE FIRST COLUMN INDICATES THE ELECTRONIC TRANSITION WITH CORRESPONDING PHONON MOMENTUM. PARAMETERS OF MoS₂ (OTHER MATERIALS) ARE TAKEN FROM [30] ([31]). AS DISCUSSED IN [30], [31], THE ENERGY VALUES FOR ACOUSTIC (OPTICAL) PHONON MODES ARE THE AVERAGE OF PHONON ENERGIES OF THE TRANSVERSE AND LONGITUDINAL (TRANSVERSE, LONGITUDINAL, AND HOMOPOLAR) MODES. IT SHOULD BE NOTICED THAT SEVERAL PHONON-ASSISTED TRANSITIONS HAVE THE SAME ENERGY BECAUSE THEY CORRESPOND TO THE SAME PHONON WAVE-VECTOR

Electron Transition		Deformation Potentials, Phonon energy				Unit
		MoS ₂	MoSe ₂	WS ₂	WSe ₂	
K→K(Γ)	$D_{ac,1}$	4.5	3.4	3.2	3.2	[eV]
K→K(Γ)	$D_{op,0}$	5.8	5.2	3.1	2.3	10 ⁸ [eV/cm]
	$\hbar\omega_{op}$	49.5	34.3	46.8	30.7	[meV]
K→K'(K)	$D_{ac,0}$	1.4	1.8	1.2	1.3	10 ⁸ [eV/cm]
	$\hbar\omega_{ac}$	26.1	18.2	20.5	16.8	[meV]
K→K'(K)	$D_{op,0}$	2.0	2.1	1.1	0.8	10 ⁸ [eV/cm]
	$\hbar\omega_{op}$	46.8	32.8	45.0	29.7	[meV]
K→Q(Q)	$D_{ac,0}$	0.93	0.91	0.73	0.82	10 ⁸ [eV/cm]
	$\hbar\omega_{ac}$	20.7	15.1	17.7	12.9	[meV]
K→Q(Q)	$D_{op,0}$	1.9	1.7	0.9	0.8	10 ⁸ [eV/cm]
	$\hbar\omega_{op}$	48.1	33.7	45.9	30.1	[meV]
K→Q(M)	$D_{ac,0}$	4.4	4.5	3.4	5.7	10 ⁸ [eV/cm]
	$\hbar\omega_{ac}$	24.2	18.0	19.6	15.8	[meV]
K→Q(M)	$D_{op,0}$	5.6	5.3	2.7	3.2	10 ⁸ [eV/cm]
	$\hbar\omega_{op}$	47.5	33.7	45.8	30	[meV]
Q→Q(Γ)	$D_{ac,1}$	2.8	3.1	1.8	1.9	[eV]
Q→Q(Γ)	$D_{op,0}$	7.1	7.8	3.4	2.7	10 ⁸ [eV/cm]
	$\hbar\omega_{op}$	49.5	34.3	46.8	30.7	[meV]
Q→Q(Q)	$D_{ac,0}$	2.1	2.2	1.7	2.7	10 ⁸ [eV/cm]
	$\hbar\omega_{ac}$	20.7	15.1	17.7	12.9	[meV]
Q→Q(Q)	$D_{op,0}$	4.8	4.3	2.3	1.9	10 ⁸ [eV/cm]
	$\hbar\omega_{op}$	48.1	33.7	45.9	30.1	[meV]
Q→Q(M)	$D_{ac,0}$	2.0	2.2	1.5	1.5	10 ⁸ [eV/cm]
	$\hbar\omega_{ac}$	24.2	18.0	19.6	15.8	[meV]
Q→Q(M)	$D_{op,0}$	4.0	5.9	1.9	1.6	10 ⁸ [eV/cm]
	$\hbar\omega_{op}$	47.5	33.7	45.8	30.0	[meV]
Q→Q(K)	$D_{ac,0}$	4.8	4.1	3.7	4.2	10 ⁸ [eV/cm]
	$\hbar\omega_{ac}$	26.1	18.2	20.5	16.8	[meV]
Q→Q(K)	$D_{op,0}$	6.5	4.7	3.1	2.5	10 ⁸ [eV/cm]
	$\hbar\omega_{op}$	46.8	32.8	45.0	29.7	[meV]
Q→K(Q)	$D_{ac,0}$	1.5	1.5	1.4	1.6	10 ⁸ [eV/cm]
	$\hbar\omega_{ac}$	20.7	15.1	17.7	12.9	[meV]
Q→K(Q)	$D_{op,0}$	2.4	3.0	1.3	1.0	10 ⁸ [eV/cm]
	$\hbar\omega_{op}$	48.1	33.7	45.9	30.1	[meV]
Q→K'(M)	$D_{ac,0}$	4.4	4.9	4.0	4.1	10 ⁸ [eV/cm]
	$\hbar\omega_{ac}$	24.2	18.0	19.6	15.8	[meV]
Q→K'(M)	$D_{op,0}$	6.6	8.3	4.6	2.8	10 ⁸ [eV/cm]
	$\hbar\omega_{op}$	47.5	33.7	45.8	30.0	[meV]

correspond to quite different phonon wave vectors $q = |\vec{k} - \vec{k}'|$. The corresponding phonon wave vectors are shown in Fig. 2(b) and (c), and for intrinsic phonon scatterings,

TABLE II

PARAMETERS FOR THE DIELECTRIC MATERIALS AND CORRESPONDING CALCULATED SO PHONON FREQUENCIES $\hbar\omega_{SO,tox}$ AND $\hbar\omega_{SO,box}$. BACK OXIDE IS SiO₂. DIELECTRIC PARAMETERS ARE TAKEN FROM [36], EXCEPT THE PARAMETERS OF BN WHICH ARE TAKEN FROM [37]

Mater.	SiO ₂	BN	AlN	Al ₂ O ₃	HfO ₂	ZrO ₂	Unit
ϵ_{tox}^0	3.9	5.09	9.14	12.53	23	24	
ϵ_{tox}^∞	2.5	4.1	4.8	3.2	5.03	4	
$\omega_{TO,tox}$	55.6	93.07	81.4	48.18	12.4	16.67	meV
$\omega_{SO,tox}$ (cal.)	69.4	100.5	104.3	83.9	21.3	30.5	meV
$\omega_{SO,box}$ (cal.)	69.4	60.1	58.0	54.2	61.1	62.9	meV

we adopted the deformation potentials and phonon energies from [30], [31], that for completeness are reported in Table I.

A remote phonon or surface-optical (SO) phonon is another important scattering source that can severely degrade electron mobility. The source of this scattering is in the surrounding dielectrics via long-range Coulomb interactions, provided that the dielectrics support polar vibrational modes. By assuming semi-infinite top and back oxides and neglecting the possible coupling to the plasmons of the 2-D material, the energy dispersion of the SO phonons can be obtained by solving the secular equation [32]

$$(\epsilon_{box}(\omega) + \epsilon_{2-D})(\epsilon_{tox}(\omega) + \epsilon_{2-D}) - (\epsilon_{box}(\omega) - \epsilon_{2-D})(\epsilon_{tox}(\omega) - \epsilon_{2-D})e^{-2qa} = 0 \quad (4)$$

where ϵ_{2-D} is the dielectric constant of the 2-D material (single-layer TMDs in this paper) [29], [33]–[35], while the indices box and tox denote the back oxide and the top oxide, respectively. A numerical solution of (4) shows that the frequency of the remote phonons has a very weak dependence on q , that consequently we neglected in our calculations by setting $e^{-2qa} \approx 1$ in (4). With this approximation, (4) simplifies to $\epsilon_{box}(\omega) + \epsilon_{tox}(\omega) = 0$, that we solved using the single polar phonon expression for the $\epsilon_{ox}(\omega)$ in each oxide

$$\epsilon_{ox}(\omega) = \epsilon^\infty + \frac{\epsilon^0 - \epsilon^\infty}{1 - \omega^2/\omega_{TO}^2} \quad (5)$$

where ϵ^∞ and ϵ^0 are the high- and low-frequency dielectric constants, respectively, and ω_{TO} is the frequency of the polar phonon in the oxide. The parameters of dielectric materials that are studied in this paper and the corresponding calculated SO phonon frequencies are reported in Table II.

The scattering matrix element of the remote phonons can be written as

$$M_{SO,tox}(\vec{k}, \vec{k}') = \sqrt{\frac{\hbar\omega_{SO,tox}}{2Sq}} \sqrt{\left(\frac{1}{\epsilon_{tox}^\infty + \epsilon_{box}(\omega_{SO,tox})} - \frac{1}{\epsilon_{tox}^0 + \epsilon_{box}(\omega_{SO,tox})} \right)} \quad (6)$$

where $\omega_{SO,tox}$ and $\omega_{SO,box}$ are the frequencies of the SO phonon from the top and back oxides, ϵ^∞ and ϵ^0 are the high- and low-frequency dielectric constants, and S is

the normalization area [32]. The scattering matrix element of the remote phonon from the back oxide is obtained by exchanging the subindex of tox and box in (6). Scattering with the SO phonon mode is inelastic and we consider only intravalley transitions.

The charged impurities located in the center of the 2-D material are another source for intravalley scattering. The 2-D Fourier transform of the scattering potential due to a charged impurity located at $(\vec{r}, z) = (0, a/2)$ can be written as [38]

$$\phi(q, z) = \frac{e^2}{2q\epsilon_{2-D}} [e^{-q|z-a/2|} + Ce^{qz} + De^{-qz}] \quad (7)$$

where e is the elementary charge, C and D are the parameters that depend on the physical properties of the dielectrics and the 2-D material [20], [38]. Thus the matrix elements due to the charge impurity scattering take the form [20]

$$M_{cb}^{(0)}(\vec{k}, \vec{k}') = \frac{e^2}{qa\epsilon_{2-D}} \left(\frac{1}{q} - \frac{q}{q^2 + (2\pi/a)^2} \right) \times \left[\frac{C}{2} (e^{qa} - 1) + \frac{D}{2} (1 - e^{-qa}) - e^{-qa/2} \right] + \frac{e^2}{qa\epsilon_{2-D}} \left(\frac{1}{q} + \frac{q}{q^2 + (2\pi/a)^2} \right). \quad (8)$$

In this paper, the effect of static screening produced by the electrons in the conduction band is described by using the dielectric function approach [38], so that the screened matrix element $M_{scr}^w(\vec{k}, \vec{k}')$ in the valley w is obtained by solving the linear problem

$$M^v(q) = \sum_w \epsilon^{v,w}(q) M_{scr}^w(q) \quad (9)$$

where v and $w \in K, Q$, $M^v(q)$ is the unscreened matrix element, and $\epsilon^{v,w}$ is the dielectric matrix calculated numerically as explained in [38]. Screening has been used for the scattering due to the charged impurities and the SO phonons, while intrinsic phonon transitions are assumed unscreened [20].

As will be discussed in the next section, the bandstructure close to the Q -valley is not isotropic and the corresponding mobility shows direction dependence, while the bandstructure close to the K -valley is taken isotropic instead. Assuming a nonparabolic dispersion relation $E(1 + \alpha E) = \hbar^2 k_i^2 / 2m_i^* + \hbar^2 k_t^2 / 2m_t^*$, the longitudinal m_l^* and transverse m_t^* effective masses, and also the nonparabolicity factor α , are extracted from the DFT-calculated electronic bandstructure.

The longitudinal direction of the Q -valley is neither the armchair nor the zigzag direction. Therefore, θ is introduced as the angle describing the valley orientation with respect to the armchair direction in real space, see Fig. 2(a). The mobility of each valley along the armchair $\mu_A^{(v)}$ and zigzag $\mu_Z^{(v)}$ direction is given by [38]

$$\begin{aligned} \mu_A^{(v)} &= \mu_{ll}^{(v)} \cos^2(\theta_v) + \mu_{tt}^{(v)} \sin^2(\theta_v) \\ \mu_Z^{(v)} &= \mu_{ll}^{(v)} \sin^2(\theta_v) + \mu_{tt}^{(v)} \cos^2(\theta_v) \end{aligned} \quad (10)$$

where θ_v is the angle of longitudinal direction of the valley v with respect to the armchair direction in real space.

TABLE III

COMPARISON OF THE CALCULATED MOBILITY IN THIS PAPER WITH THE EXPERIMENTAL DATA OF [10]. $T = 100$ K AND THE IMPURITY DENSITY IS $4 \times 10^{12} \text{ cm}^{-2}$. THE UNITS OF CARRIER CONCENTRATION (n) AND MOBILITY (μ) ARE cm^{-2} AND $\text{cm}^2/(\text{Vs})$, RESPECTIVELY

n	7.6×10^{12}	9.6×10^{12}	1.15×10^{13}	1.35×10^{13}
μ (Cal.)	93	106	114	122
μ (Exp.)	96 ± 3	111 ± 3	128 ± 3	132 ± 3

ll and tt denote the mobility, respectively, in the longitudinal and transverse direction of the valley v . The θ angle for the valleys Q has a very weak dependence on the biaxial strain and is approximately zero for two of the Q -valleys, is $\pi/3$ for other two of them, and is $2\pi/3$ for the remaining Q -valleys. The overall mobility does not depend on the direction and is obtained as the average of the mobilities in different valleys weighted by the corresponding electron density [20]. The low-field mobility can be calculated by solving numerically the linearized BTE, which in previous works has been almost universally solved in approximated forms [38]. In this paper, instead, we have employed an energy driven discretization method described in [20], [21] that allows one to write the discretized BTE in the form of a linear, algebraic problem, and provides detailed expressions in terms of scattering matrix elements for the entries of the matrix governing the linear problem. In this approach, multiple scattering mechanisms are naturally included by adding the corresponding scattering rates before the calculation of the momentum relaxation time without resorting to the semiempirical Matthiessen's rule for the relaxation times [21]. Table III compares our calculated mobilities at various carrier concentrations with the experimental data reported in [10] for the unstrained single-layer MoS₂ embedded between SiO₂ and HfO₂ with an impurity density equal to $4 \times 10^{12} \text{ cm}^{-2}$ at $T = 100$ K. A very good agreement with experimental data validates the bandstructure and mobility models employed in this paper.

III. RESULTS AND DISCUSSIONS

Fig. 3(a)–(d) shows the bandstructure of the unstrained and strained single-layer MoS₂, MoSe₂, WS₂, and WSe₂. A tensile biaxial strain increases the energy distance between the K - and Q -valleys, whereas under a small compressive strain this energy distance is reduced. With a further increase of compressive strain, the Q -valley will be the lowest one and the K -valley will not significantly contribute to the electron mobility. The energy distances between the K - and Q -valleys reported in this paper and in some previous contributions are compared in Table IV. Except for MoS₂, where experiments indicate an energy distance larger than 60 meV [26], for the other materials, this parameter has not been experimentally extracted. Fig. 4 shows the evaluated energy minima of the valleys as a function of strain for the discussed materials. A small tensile strain of 0.4% increases the energy distance by more than 150 meV, which can effectively enhance the mobility because of the reduction of intervalley phonon scattering. The compressive strain, however, decreases this

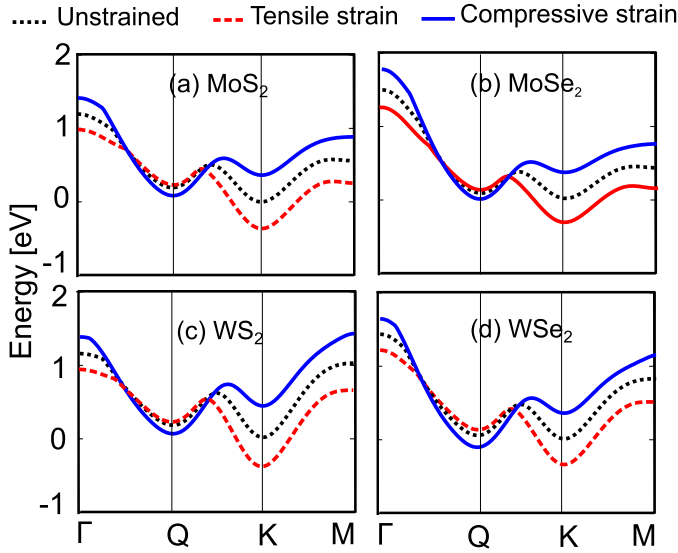


Fig. 3. Band structure of unstrained (black line), under compressive strain (blue line), and under tensile strain (red line) of single-layer (a) MoS₂, (b) MoSe₂, (c) WS₂, and (d) WSe₂. The strain magnitude is 2.5% in all strained cases.

TABLE IV

ENERGY DISTANCES BETWEEN *K*- AND *Q*-VALLEYS BASED ON THEORETICAL STUDIES IN [23], [24], [31]. THE UNITS ARE meV

Mater.	K and Q-Valley Energy Distance [meV]			
	This Study	Ref. [31]	Ref. [23]	Ref. [24]
MoS ₂	195	81	300 ± 30	255 ± 10
MoSe ₂	72	28	370 ± 30	180 ± 10
WS ₂	166	67	80 ± 30	200 ± 10
WSe ₂	48	16	220 ± 30	135 ± 10

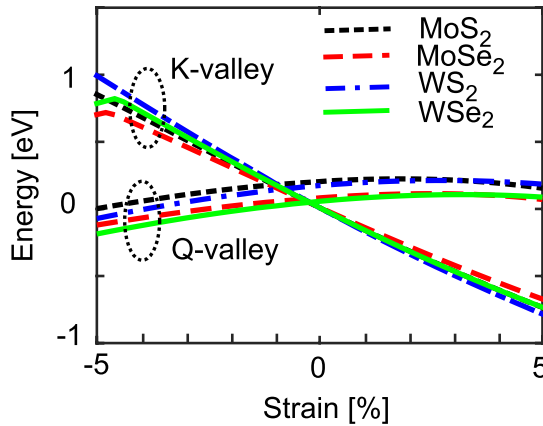


Fig. 4. Energy minima of the *K*- and *Q*-valleys under biaxial strain for MoS₂ (black), MoSe₂ (red), WS₂ (blue), and WSe₂ (green) (see Fig. 1 and Fig. 2).

energy distance and with a relatively large compressive strain the *Q*-valley becomes the lowest valley. The longitudinal m_l^* and transverse m_t^* effective masses and the nonparabolicity factors α are shown in Fig. 5(a)–(d). The effective masses of the unstrained WS₂ and WSe₂ are smaller than that of the unstrained MoS₂ and MoSe₂. In all cases, a tensile strain decreases the effective mass of the *K*-valley while a compressive strain reduces the effective mass of the *Q*-valley.

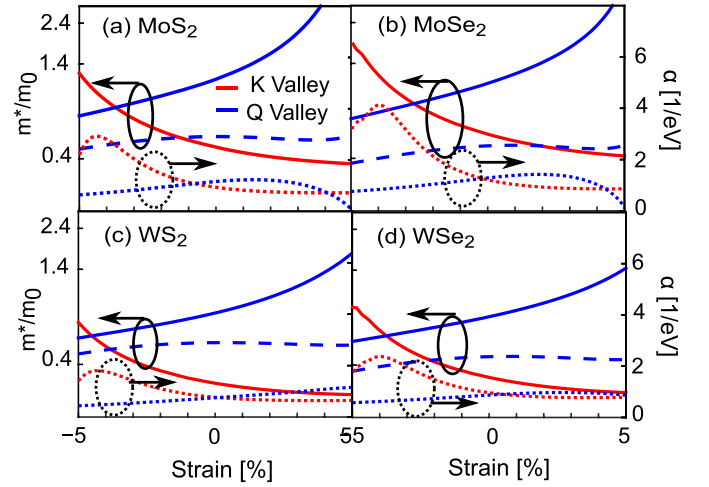


Fig. 5. Effective masses (solid-lines for longitudinal and dashed-lines for transverse mass) and the nonparabolicity factors (α) (dotted-lines) of various valleys (blue line for *K*-valley and red line for *Q*-valley) under biaxial strain for (a) MoS₂, (b) MoSe₂, (c) WS₂, and (d) WSe₂. The longitudinal and transverse effective masses of *K*-valley have been found to be essentially equal.

The strain dependence of intrinsic phonon-limited mobility is presented in Fig. 6(a). There is a general trend for the modulation of mobility with the strain for all discussed materials, which can be explained by the variation of intervalley scattering between the *K*- and *Q*-valleys with strain. As the mobility enhancement with the tensile strain is due to the reduction of intervalley scattering, the TMDs with a relatively small energy distance between the *K*- and *Q*-valleys will show a large mobility enhancement with the small tensile strain. For example, the energy distances between the valleys for MoSe₂ and WSe₂ are 72 meV and 48 meV, respectively, and a tensile strain of 0.4% results in 64% and 296% mobility enhancement compared with the unstrained materials. The mobility enhancement for MoS₂ and WS₂ under the same condition is 9% and 8%, which is due to their relatively large *K* to *Q* valleys energy distance of 195 meV and 166 meV, respectively. The mobilities of WS₂ and WSe₂ are the highest in comparison with the other TMDs because of the relatively small effective mass of the *Q*-valley under the tensile strain.

To explain the strong variation of mobility with a small compressive strain, Fig. 6(b) shows the fraction of carrier concentration of the *K*- and *Q*-valleys as a function of strain. As can be seen, under tensile strain the *Q*-valley becomes empty and does not contribute to electronic conduction, while under the compressive strain the carrier concentration of the *Q*-valley increases and this valley dominates the electron transport. As the effective mass of the *Q*-valley is larger than that of the *K*-valley, the phonon limited mobility of this valley is smaller than that of the *K*-valley, see Fig. 6(c). As can be seen in Fig. 6(c), because of decreasing the intervalley phonon scattering, the small tensile strain increases significantly the mobility of *K*-valley. The minimum of the overall mobility occurs as the energy minima of the *K*- and *Q*-valleys get very close to each other and the intervalley scattering is thus maximum.

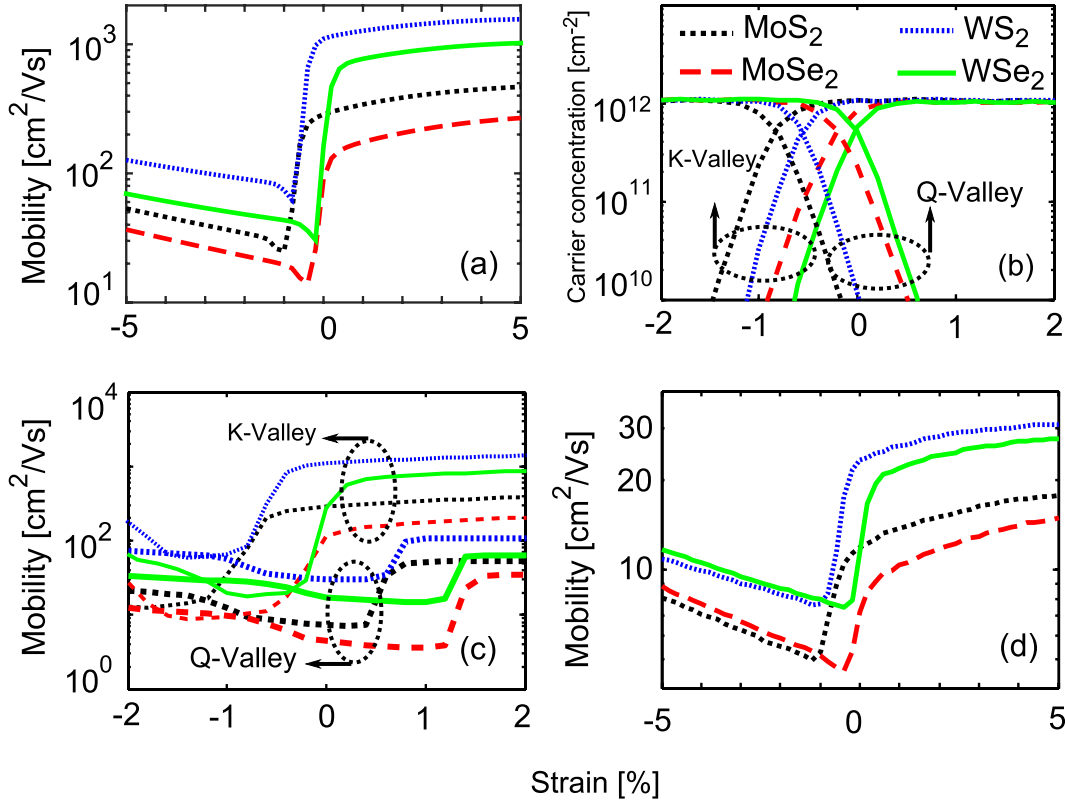


Fig. 6. (a) Phonon limited mobility of single-layer TMDs as a function of strain with a carrier concentration of $n = 10^{12} \text{ cm}^{-2}$. (b) and (c) Fraction of carrier concentration and phonon limited mobility of K - and Q -valleys of single-layer TMDs as a function of strain. (d) Mobility limited by intrinsic phonon modes, remote phonon, and screened charged impurity scattering with SiO_2 as the back oxide ($\epsilon_r = 3.9$) and HfO_2 as the top oxide ($\epsilon_r = 23$). Carrier and charged impurity concentrations are equal to $n = n_{\text{imp}} = 10^{12} \text{ cm}^{-2}$. Black, red, blue, and green lines illustrate the mobility of MoS_2 , MoSe_2 , WS_2 , and WSe_2 , respectively.

Fig. 6(d) shows the mobility in the presence of the intrinsic phonon, remote phonon, and charged impurity scattering. The top and back oxides are assumed to be HfO_2 and SiO_2 , respectively, and both the carrier and impurity concentrations are 10^{12} cm^{-2} . As the charge impurity and remote phonon scattering result in intravalley transitions, which are weakly affected by the strain, the mobility enhancement by strain in the presence of these scattering mechanisms is smaller than it is for the phonon limited mobility. In this case, the mobility enhancements under 0.4% tensile strain are about 5%, 27%, 4%, and 84% for MoS_2 , MoSe_2 , WS_2 , and WSe_2 , respectively.

The room temperature mobility of the discussed materials at various carrier concentrations is compared in Fig. 7 for both the unstrained and strained conditions. A relatively small tensile strain of 0.4% only weakly affects the effective mass of the K -valley (lowest valley), while it has a stronger effect on the energy distance of the valleys. Therefore, this small strain has the largest (smallest) effect on the mobility of single-layer WSe_2 (MoS_2), which has the minimum (maximum) energy distance between the valleys. As at higher carrier concentrations, the remote phonon and charged impurity scattering are strongly screened and the intrinsic phonon scattering plays a more significant role on the mobility, the mobility enhancement by strain is more pronounced at relatively high carrier concentrations. The unstrained single-layer WSe_2 has the smallest mobility among all of

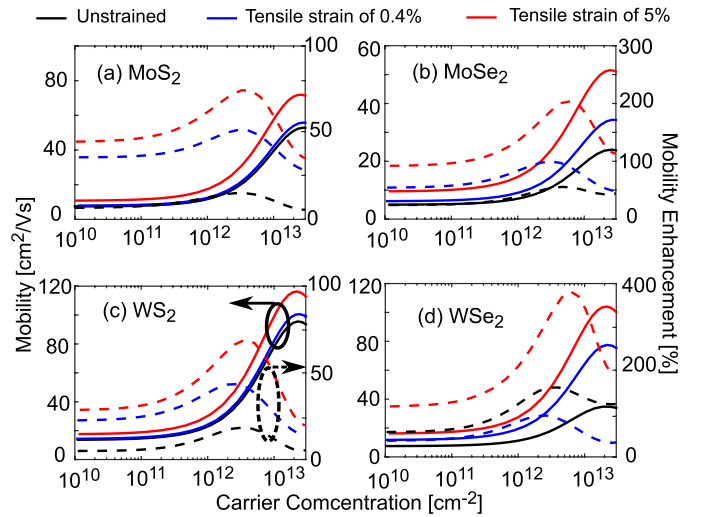


Fig. 7. Mobility (solid lines) and mobility enhancement (dashed lines) with the inclusion of intrinsic phonon, remote phonon, and charged impurity scattering for the unstrained (black), under a tensile biaxial strain of 0.4% (blue), under a tensile biaxial strain of 5% (red) for (a) MoS_2 , (b) MoSe_2 , (c) WS_2 , and (d) WSe_2 . Top and back oxide are HfO_2 and SiO_2 , respectively, and the charge impurity concentration is equal to $n_{\text{imp}} = 10^{12} \text{ cm}^{-2}$. Left axes: mobility. Right axes: mobility enhancement.

the discussed unstrained materials, while it has the largest mobility enhancement with a tensile strain in the range of 0.4%–5% and it achieves the highest mobility under a tensile strain of 5%.

IV. CONCLUSION

A theoretical study on the role of strain on the mobility of the single-layer MoS₂, MoSe₂, WS₂, and WSe₂ is presented. The DFT calculations are used to obtain the effective masses and energy minima of the contributing valleys. The linearized BTE is solved for evaluating the mobility, including the effects of the intrinsic phonons, remote phonons, and screened charged impurities. The results indicate that, a tensile strain increases the mobility, whereas a compressive strain reduces the mobility. The unstrained mobility and the mobility enhancement with a strain strongly depend on the energy distance between the *K*- and *Q*-valleys. A small tensile strain has a higher impact on the mobility of materials with a smaller energy distance between the valleys, such as MoSe₂ and WSe₂. Various energy distance values result in similar mobility characteristics and only change the strain value at which the mobility starts to increase. Therefore, the main conclusion of this paper remains valid regardless of the exact value of the energy distance between the *K*- and *Q*-valleys. The results pave the way for improving the performance of TMD-based electronic devices by strain engineering.

REFERENCES

- [1] K. S. Novoselov *et al.*, "Electric field effect in atomically thin carbon films," *Science*, vol. 306, no. 5696, pp. 666–669, 2004.
- [2] C. R. Dean *et al.*, "Boron nitride substrates for high-quality graphene electronics," *Nature Nanotechnol.*, vol. 5, no. 10, pp. 722–726, 2010.
- [3] Y. Zhang *et al.*, "Direct observation of a widely tunable bandgap in bilayer graphene," *Nature*, vol. 459, no. 7248, pp. 820–823, 2009.
- [4] P. Gava, M. Lazzeri, A. M. Saitta, and F. Mauri, "Ab initio study of gap opening and screening effects in gated bilayer graphene," *Phys. Rev. B*, vol. 79, no. 16, p. 165431, Apr. 2009.
- [5] A. H. C. Neto and K. Novoselov, "New directions in science and technology: Two-dimensional crystals," *Rep. Prog. Phys.*, vol. 74, no. 8, pp. 082501-1–082501-9, 2011.
- [6] K. S. Novoselov *et al.*, "Two-dimensional atomic crystals," *Proc. Nat. Acad. Sci. USA*, vol. 102, no. 30, pp. 10451–10453, 2005.
- [7] A. Ayari, E. Cobas, O. Ogundadege, and M. S. Fuhrer, "Realization and electrical characterization of ultrathin crystals of layered transition-metal dichalcogenides," *J. Appl. Phys.*, vol. 101, no. 1, p. 014507, 2007.
- [8] H. S. S. Ramakrishna Matt *et al.*, "MoS₂ and WS₂ analogues of graphene," *Angew. Chem. Int. Ed.*, vol. 49, no. 24, pp. 4059–4062, 2010.
- [9] B. Radisavljevic, A. Radenovic, J. Brivio, V. Giacometti, and A. Kis, "Single-layer MoS₂ transistors," *Nature Nanotechnol.*, vol. 6, no. 3, pp. 147–150, 2011.
- [10] B. Radisavljevic and A. Kis, "Mobility engineering and a metal–insulator transition in monolayer MoS₂," *Nature Mater.*, vol. 12, no. 9, pp. 815–820, 2013.
- [11] S. Larentis, B. Fallahazad, and E. Tutuc, "Field-effect transistors and intrinsic mobility in ultra-thin MoSe₂ layers," *Appl. Phys. Lett.*, vol. 101, no. 22, p. 223104, 2012.
- [12] D. Ovchinnikov, A. Allain, Y.-S. Huang, D. Dumcenco, and A. Kis, "Electrical transport properties of single-layer WS₂," *ACS Nano*, vol. 8, no. 8, pp. 8174–8181, 2014.
- [13] W. Liu, J. Kang, D. Sarkar, Y. Khatami, D. Jena, and K. Banerjee, "Role of metal contacts in designing high-performance monolayer n-type WSe₂ field effect transistors," *Nano Lett.*, vol. 13, no. 5, pp. 1983–1990, 2013.
- [14] M. Li, D. Esseni, G. Snider, D. Jena, and H. G. Xing, "Single particle transport in two-dimensional heterojunction interlayer tunneling field effect transistor," *J. Appl. Phys.*, vol. 115, no. 7, p. 074508, 2014.
- [15] H. Shi, H. Pan, Y.-W. Zhang, and B. I. Yakobson, "Quasiparticle band structures and optical properties of strained monolayer MoS₂ and WS₂," *Phys. Rev. B*, vol. 87, no. 15, p. 155304, Apr. 2013.
- [16] H. J. Conley, B. Wang, J. I. Ziegler, R. F. Haglund, Jr., S. T. Pantelides, and K. I. Bolotin, "Bandgap engineering of strained monolayer and bilayer MoS₂," *Nano Lett.*, vol. 13, no. 8, pp. 3626–3630, 2013.
- [17] S. M. Tabatabaei, M. Noei, K. Khaliqi, M. Pourfath, and M. Fathipour, "A first-principles study on the effect of biaxial strain on the ultimate performance of monolayer MoS₂-based double gate field effect transistor," *J. Appl. Phys.*, vol. 113, no. 16, p. 163708, 2013.
- [18] J. Feng, X. Qian, C.-W. Huang, and J. Li, "Strain-engineered artificial atom as a broad-spectrum solar energy funnel," *Nature Photon.*, vol. 6, no. 12, pp. 866–872, 2012.
- [19] M. Ghorbani-Asl, S. Borini, A. Kuc, and T. Heine, "Strain-dependent modulation of conductivity in single-layer transition-metal dichalcogenides," *Phys. Rev. B*, vol. 87, no. 23, p. 235434, Jun. 2013.
- [20] M. Hosseini, M. Elahi, M. Pourfath, and D. Esseni, "Strain induced mobility modulation in single-layer MoS₂," *J. Phys. D: Appl. Phys.*, vol. 48, no. 37, p. 375104, 2015.
- [21] A. Paussa and D. Esseni, "An exact solution of the linearized Boltzmann transport equation and its application to mobility calculations in graphene bilayers," *J. Appl. Phys.*, vol. 113, no. 9, p. 093702, 2013.
- [22] J. M. Soler *et al.*, "The SIESTA method for *ab initio* order-*N* materials simulation," *J. Phys.: Condens. Matter*, vol. 14, no. 11, p. 2745, 2002.
- [23] A. Kumar and P. K. Ahluwalia, "Electronic structure of transition metal dichalcogenides monolayers 1H-MX₂ (M = Mo, W; X = S, Se, Te) from *ab-initio* theory: New direct band gap semiconductors," *Eur. Phys. J. B*, vol. 85, no. 6, pp. 186-1–186-7, 2012.
- [24] C.-H. Chang, X. Fan, S.-H. Lin, and J.-L. Kuo, "Orbital analysis of electronic structure and phonon dispersion in MoS₂, MoSe₂, WS₂, and WSe₂ monolayers under strain," *Phys. Rev. B*, vol. 88, no. 19, p. 195420, Nov. 2013.
- [25] A. Ramasubramaniam, "Large excitonic effects in monolayers of molybdenum and tungsten dichalcogenides," *Phys. Rev. B*, vol. 86, no. 11, p. 115409, Sep. 2012.
- [26] T. Eknepakul *et al.*, "Electronic structure of a quasi-freestanding MoS₂ monolayer," *Nano Lett.*, vol. 14, no. 3, pp. 1312–1316, 2014.
- [27] K. Kaasbjerg, K. S. Thygesen, and A.-P. Jauho, "Acoustic phonon limited mobility in two-dimensional semiconductors: Deformation potential and piezoelectric scattering in monolayer MoS₂ from first principles," *Phys. Rev. B*, vol. 87, p. 235312, Jun. 2013.
- [28] N. Ma and D. Jena, "Charge scattering and mobility in atomically thin semiconductors," *Phys. Rev. X*, vol. 4, no. 1, p. 011043, Mar. 2014.
- [29] Q. Yue *et al.*, "Mechanical and electronic properties of monolayer MoS₂ under elastic strain," *Phys. Lett. A*, vol. 376, nos. 12–13, pp. 1166–1170, 2012.
- [30] X. Li, J. T. Mullen, Z. Jin, K. M. Borysenko, M. B. Nardelli, and K. W. Kim, "Intrinsic electrical transport properties of monolayer silicene and MoS₂ from first principles," *Phys. Rev. B*, vol. 87, no. 11, p. 115418, Mar. 2013.
- [31] Z. Jin, X. Li, J. T. Mullen, and K. W. Kim, "Intrinsic transport properties of electrons and holes in monolayer transition-metal dichalcogenides," *Phys. Rev. B*, vol. 90, no. 4, p. 045422, Jul. 2014.
- [32] Z.-Y. Ong and M. V. Fischetti, "Theory of remote phonon scattering in top-gated single-layer graphene," *Phys. Rev. B*, vol. 88, p. 045405, Jul. 2013.
- [33] H. Fang, S. Chuang, T. C. Chang, K. Takei, T. Takahashi, and A. Javey, "High-performance single layered WSe₂ p-FETs with chemically doped contacts," *Nano Lett.*, vol. 12, no. 7, pp. 3788–3792, 2012.
- [34] R. A. Gordon, D. Yang, E. D. Crozier, D. T. Jiang, and R. F. Frindt, "Structures of exfoliated single layers of WS₂, MoS₂, and MoSe₂ in aqueous suspension," *Phys. Rev. B*, vol. 65, no. 12, p. 125407, Mar. 2002.
- [35] A. Kumar and P. K. Ahluwalia, "Tunable dielectric response of transition metals dichalcogenides MX₂ (M = Mo, W; X = S, Se, Te): Effect of quantum confinement," *Phys. B, Condens. Matter*, vol. 407, no. 24, pp. 4627–4634, 2012.
- [36] A. Konar, T. Fang, and D. Jena, "Effect of high- κ gate dielectrics on charge transport in graphene-based field effect transistors," *Phys. Rev. B*, vol. 82, no. 11, p. 115452, Sep. 2010.
- [37] V. Perebeinos and P. Avouris, "Inelastic scattering and current saturation in graphene," *Phys. Rev. B*, vol. 81, no. 19, p. 195442, May 2010.
- [38] D. Esseni, P. Palestri, and L. Selmi, *Nanoscale MOS Transistors: Semi-Classical Transport and Applications*. Cambridge, U.K.: Cambridge Univ. Press, 2011.